INTERNATIONAL JOURNAL FOR NUMERICAL METHODS IN FLUIDS
Int. J. Numer. Meth. Fluids 2009; **59**:1259–1283
Published online 17 July 2008 in Wiley InterScience (www.interscience.wiley.com). DOI: 10.1002/fld.1866

Modelling nasal airflow using a Fourier descriptor representation of geometry

A. M. Gambaruto, D. J. Taylor and D. J. Doorly*, †

Department of Aeronautics, Imperial College London, South Kensington Campus, London SW7 2AZ, U.K.

SUMMARY

Procedures capable of providing both compact representations and rational simplifications of complex anatomical flow conduits are essential to explore how form and function are related in the respiratory, cardiovascular and other physiological flow systems. This study focuses on flow in the human nasal cavity. Methods to derive the cavity wall boundary from medical images are first outlined. Anisotropic smoothing of the boundary surface is shown to provide less geometric distortion in regions of high curvature, such as at the ends of the narrow nasal passages. A reversible decomposition of the surface into a stack of planar contours is then effected using an implicit function formulation. Fourier descriptors provide a continuous representation of each contour as a modal expansion and permit simplification of the geometry by retaining only dominant modes via filtering.

Computations of the steady inspiratory flow field are performed for replica and reduced geometries, where reduced geometry is derived by retaining only the first 15 modes in the expansion of each slice contour. The overall pressure drop and integrated wall shear are shown to be virtually unaffected by simplification. More sensitive measures, such as the Lagrangian particle trajectories and residence time distributions, show slight changes as discussed.

Comparison of the Fourier descriptor method applied to three different patient data sets indicates the potential of the technique as a means to characterize complex flow conduit geometry, and the scope for further work is outlined. Copyright © 2008 John Wiley & Sons, Ltd.

Received 20 December 2007; Revised 13 May 2008; Accepted 25 May 2008

KEY WORDS: nasal airflow; geometry characterization and decomposition; nasal passage; anisotropic surface smoothing; implicit function; Fourier descriptors

*Correspondence to: D. J. Doorly, Department of Aeronautics, Imperial College London, South Kensington Campus, London SW7 2AZ, U.K.
†E-mail: d.doorly@imperial.ac.uk

Contract/grant sponsor: Biotechnology and Biological Sciences Research Council (BBSRC); contract/grant numbers: E18557, BB/E02344/1
Contract/grant sponsor: HPCx National Computing Resource

1. INTRODUCTION

Exploring the link between form and flow in humans is of interest both for understanding the normal physiological function and for healthcare. In medical applications, a particular objective is to understand how key geometric attributes affect the normal and pathological functions, which is helpful in the diagnosis and prognosis stages and is of paramount importance in surgical planning and other forms of aimed intervention.

Changes in the flow field with respect to variations in the geometry were studied in [1] for a peripheral bypass graft configuration, as part of a sensitivity analysis of medical image geometric reconstruction procedures and topological idealization. By introducing local variations in the graft geometry, while maintaining the global topological form, it was shown that the degree of correlation between flow and geometry changes was variable. Downstream of a stenosis (narrowing), the flow was shown to be highly sensitive to stenosis morphology, whereas in the upstream zone, good correlation between local flow and geometry changes was observed. The work presented here leads on from [1]. For the bypass graft, the orientation of vessel centreline tangents at the anastomosis, together with elliptical section fitting, was sufficient to characterize and simplify the flow conduit geometry. To represent the nasal cavity airways, however, a more general approach that also facilitates the systematic study of flow sensitivity to geometry is needed; this provides the motivation to develop improved means to describe flow conduit geometry.

As an example of how flow responds to a complex conduit geometry and, more specifically, as an illustration of how elegantly biological form controls flow in order to achieve physiological function, the nasal cavity provides a remarkably interesting study. The nasal cavity serves three principal roles: (i) it warms and humidifies inspired air; (ii) it protects and defends the lower respiratory tract by filtering particles and trapping some pathogens; and (iii) it houses the olfactory receptors [2, 3]. Filtration of particles involves deposition on the cavity walls or on the nasopharynx with nearly all particles greater than 5 μm and about 50% of those 2–4 μm captured while the majority of particles smaller than 2 μm bypass the nose [2]. Air conditioning involves both heating and humidifying the air on inspiration (23°C, 40% relative humidity at the nares to 33°C, 98% relative humidity) and recapturing some heat and humidity on expiration (37°C, 98% relative humidity to 33°C, 85% relative humidity at the nares, resulting in $\sim$100 ml of water per day being saved) [2]. The olfactory receptors are concentrated in the olfactory cleft, in the superior and posterior regions of the cavity [4].

Studies of nasal cavity airflow arise not only from the need to increase the understanding of respiratory physiology but also to provide knowledge for possible applications in surgery, drug delivery and toxicology. The nasal cavity surface is rich in blood vessels, including arterioles and capillaries [3] that allow the possibility of nasal drug delivery, as discussed in [5–7]. An advantage is the quick uptake of drugs into the circulatory system without the necessity of intravenous administration.

The location and overall extent of the nasal airways are shown in Figure 1. The morphology of the nasal airways is complex and furthermore shows wide variation both inter- and intra-individually. Intra-individual variations in passage geometry are readily produced by mucosal tissue engorgement, arising spontaneously with the nasal cycle (a temporal alteration in the degree of congestion of one side of the nose compared with that of the other) or as a reaction to an allergen or infection. Inter-individual variations are marked, with a wide variety of morphological forms observed [8, 9].

DOI: 10.1002/fld

Figure 1. Head and nasal cavity (patient Case 2) in (a) sagittal, (b) coronal and (c) axial views.

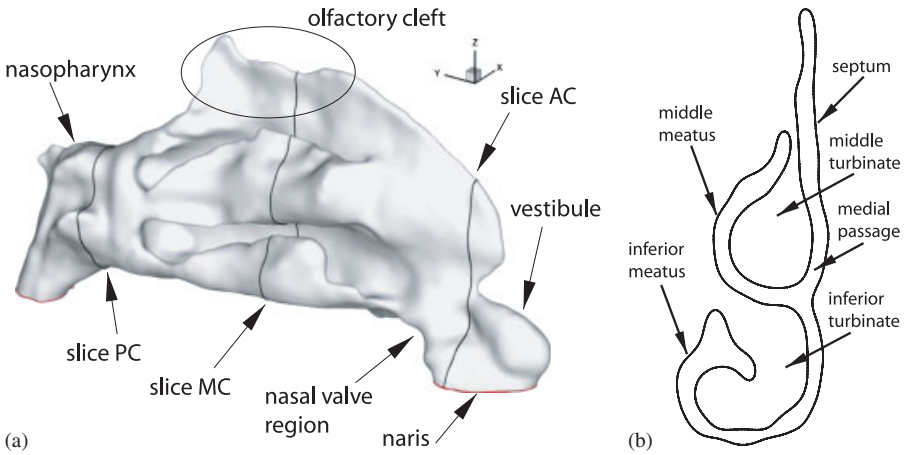

Figure 2. Nomenclature of right nasal cavity airway (patient Case 3). (a) The surface is the boundary of airway to the surrounding solid structure. The location of illustrative slices taken in the anterior (AC), middle (MC) and posterior (PC) cavity regions are also shown. (b) Slice MC is in the coronal plane.

In this study, only one-half of the nasal cavity is considered, the one on the right in Figure 2, derived from *in vivo* imaging as outlined later. Referring to the anatomical features and nomenclature indicated in Figure 2, noteworthy attributes of the geometry shown are as follows: (i) the nasal valve area, at 42 mm^2, lies at the low end of the normal range [10]; (ii) the main passageways (medial, inferior and middle meatus, respectively, approximately 1.4 mm in calibre each) are patent though of restricted calibre; and (iii) the small superior meatus is not patent in this representation, hence absent from Figure 2.

There have been a number of studies to understand how the morphology affects the flow in the human nasal cavity. One of these, [11], studies the correlation between flow resistance and geometry for a 3:1 *in vitro* model. That study finds that the pressure drop in the nasal cavity is dependent largely on three characteristic dimensions for each of the three sections of the nasal cavity: anterior, middle and posterior, comprising the geometry from the nares to the start of the turbinates, the region of the turbinates and finally the nasopharynx, respectively. In the anterior section the constriction of the nasal valve is the dominating feature, in the middle section the

DOI: 10.1002/fld

passage width and finally in the posterior section it is the sharp bend to redirect the flow, which causes the largest pressure drops.

Pressure gradient by itself provides little or no information on the partitioning of airflow within the nasal cavity, or on important functional quantities such as local wall shear stress (WSS) or particle transport. Studies that describe the airflow in detail have predominantly utilized a single model anatomy. A variety of airflow patterns have been found, according to the specific details of the particular morphology. However, Churchill *et al*. [8] performed *in vitro* studies using 10 geometries to identify a correlation of basic geometric parameters with the transitional flow rate; they found moderate or poor correlation with each parameter chosen, demonstrating the complex nature of the flow in the nasal airway. A numerical patient-specific study with different amounts of congestion applied to the virtual model is studied in [4], with modeling of nasal odorant transport as a sensitive indicator of differences in the flow. They discern that small changes in specific regions of the geometry can cause large changes in the airflow and the odorant uptake.

Other studies [12, 13] have contrasted the patient-specific analysis with a nose-like model that tries to encapsulate the essential features of the nasal cavity and with a replica anatomical configuration [14, 15]. The simplified models described utilize a box-like geometry, with the turbinates idealized as simple projections of tapered rectangular cross section. Such studies seek to obtain essential flow features to compare flow in real and idealized models.

Taken together, these studies represent the first steps in studying nasal airflow in the human based on sampled topological characteristics. Previous works however lacked the tools needed to simplify or rationalize the airways or to systematically compare anatomical form except in an *ad hoc* manner. A rationalized description of the passageways is presented here to provide a compact, hierarchical description of a single anatomy, and as a means to quantify inter-patient variations in morphology. This study presents the basic technique and illustrates its application to two different problems. In the first problem, the sensitivity of the flow to a reduced model is examined, where the emphasis is on preserving detailed topology, while keeping the representation compact. For this problem, computations with high spatial resolution are used to derive the local and regionally averaged WSS and Lagrangian marker particle distributions, which are sensitive measures of flow. The second problem briefly describes how the technique may be applied to compare and combine different nasal anatomies.

The proposed approach to study the nasal cavity requires an anatomically realistic 3D virtual model. This is obtained by reconstructing the geometry from a stack of computed tomography (CT) images obtained *in vivo*. Subsequently, an implicit function formulation is employed to define the geometry surface and is achieved by using radial basis function (RBF) interpolation of selected cross-sectional slices of the geometry surface. Since the geometry is defined by the interpolation of these selected slices, they, in fact, contain sufficient information to describe the morphology. The stack of cross sections is finally studied by the use of Fourier descriptors that characterize the geometry. The process is reversible largely within pixel resolution and hence within the bounds of the original medical image uncertainty. With the set of Fourier descriptors the geometry surface can be obtained; hence, the descriptors contain sufficient information to describe the morphology.

Fourier descriptors have previously been used in the field of shape recognition and discrimination [16]. Their use in medical applications includes probabilistic models for 2D medical image segmentation of the distal femur [17] and the left ventricle during cardiac motion [18] as well as for classifying different shapes of the corpus callus in 2D [19] and 3D [20]. 2D Fourier descriptors have further shown feasibility in distinguishing between benign and malignant breast tumours from mammograms in [21, 22] as well as in analysing blood cell types from blood samples in order to

DOI: 10.1002/fld

identify malignant cells and distinguish between lymphomas and leukaemia [23]. Other than the related studies of [24, 25], this appears to be the first application of Fourier descriptors to the nasal cavity geometry.

The outline of this paper is as follows. Section 2 presents the virtual model reconstruction from medical images including the smoothing procedure to obtain an anatomically realistic virtual model. Taking an example of a patient-specific geometry, Section 3 discusses the use of Fourier descriptors to represent the airway boundary contours obtained by slicing the geometry and from which the original geometry can be reconstructed using an implicit function. By retaining only the dominant Fourier modes to describe the geometry, a reduced model anatomy may be derived. In Section 4, computational fluid dynamic (CFD) results of a patient-specific study are presented to illustrate the essential attributes of nasal airflow and to determine the effect on the flow of small boundary alterations incurred by filtering the modal expansion of the geometry. In Section 5, two further nasal cavity geometries are introduced and an inter-patient analysis using Fourier descriptors is performed. Finally, conclusions are given in Section 6.

2. NASAL CAVITY RECONSTRUCTION FROM *IN VIVO* IMAGES

Before morphological or fluid dynamic investigations of the nasal cavity can begin, the first task is to define the nasal airway boundaries from *in vivo* medical images, to ensure that the model is anatomically realistic. For the three subjects considered, the nasal airway geometry data are given in the form of a stack of medical images in grey scale obtained from *in vivo* CT and comprising the order of 80 images in the axial plane with resolution parameters: 512×512 pixels, 1.3 mm slice thickness, 0.7 mm slice spacing, 0.39×0.39 mm pixel size. The patient CT data used were obtained with permission by retrospective examination of clinical records from the ENT surgical department at St Marys Hospital, Paddington, London. A small proportion of clinically referred subjects display airway anatomies subsequently determined to be normal by a consultant radiologist. The patient case information at the time of study is as follows: Case 1, female 47 years old; Case 2, male 31 years old; Case 3, female 53 years old.

Medical image segmentation to identify the boundary of the airway and the surrounding tissue is based on an initial constant value of grey scale. A refinement to the segmentation is required to exclude secondary conduits such as those to the sinuses as well as to identify under-resolved structures, and thus to interpret the data accordingly. This refinement is based on the discretion of an experienced user and to ensure that it is performed accurately, the image stack is viewed simultaneously in the coronal, sagittal and axial planes. In Figure 3, the CT image projected in the coronal plane, corresponding to slice anterior cavity (AC), can be seen. The possibility of viewing the CT images in different orthogonal planes allows for closer inspection of the segmentation process. By segmenting along pixel boundaries, a step-like closed contour of the nasal cavity surface is obtained for each image. The contour stack is then assembled by extruding each contour by the image slice spacing so that a closed, pixelated surface mesh is obtained.

Due to the pixelated nature of the medical images, the resulting surfaces are unrealistically rough and surface smoothing is necessary. Care must be taken in the smoothing procedure to ensure fidelity with the medical images. The smoothing is performed by iteratively moving the mesh nodes using the local mesh connectivity information; the surface roughness is thus minimized, and hence the curvature variation.

DOI: 10.1002/fld

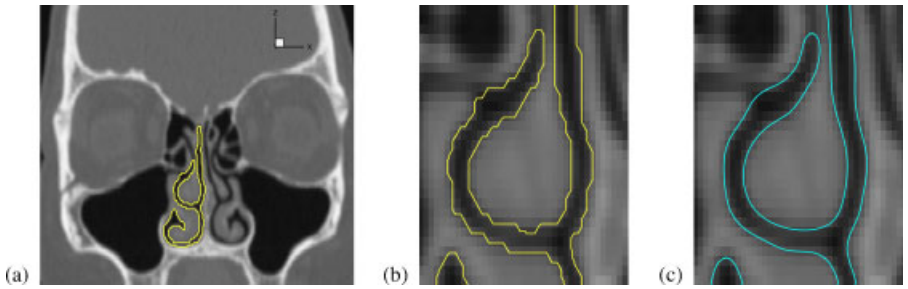

Figure 3. (a) CT image projected in the coronal place, corresponding to slice MC (middle cavity), with user-defined segmentation. Note that the sinuses and secondary conduits are excluded. Detail of the middle meatus section with (b) step-like segmentation as selected by the user and (c) reduced model (using 15 dominant Fourier modes).

Consider a regular triangular mesh consisting of n vertices $\mathbf{v}_i = (x_i, y_i, z_i);\ i = 1, \ldots, n$. The vertices neighbouring each vertex $\mathbf{v}_i$ in the triangulation are denoted by $\mathbf{v}_j; j = 1, \ldots, m_i$, where m_i is the number of neighbours. The discrete Laplacian at the vertex $\mathbf{v}_i$ is calculated as

$$\mathbf{L}_i = \sum_{j=1}^{m_i} w_{ij}(\mathbf{v}_j - \mathbf{v}_i) \tag{1}$$

where the weights w_{ij} have the constraint that $\sum_{j=1}^{m_i} w_{ij} = 1$. Here, $w_{ij} = 1/m_i$ is used, and hence the Laplacian can be interpreted as the vector moving the node in question to the barycentre of the neighbour vertices, which is known to be stable [26, 27].

The smoothing algorithm is iterative and the mesh nodes $\mathbf{v}_i^k$, where k denotes the iteration number, are moved simultaneously to a new position

$$\mathbf{v}_i^{k+1} = \mathbf{v}_i^k + \lambda \mathbf{L}_i^k, \quad 0 \leqslant \lambda \leqslant 1 \tag{2}$$

This form of smoothing is known as Laplacian smoothing and can be interpreted as an explicit iterative solution to the diffusion equation where the curvature is the property diffused. Laplacian smoothing produces large shrinkage of the surface; hence, an inflation step is introduced as

$$\begin{aligned} \mathbf{v}_i^{k+1/2} &= \mathbf{v}_i^k + \lambda \mathbf{L}_i^k \\ \mathbf{v}_i^{k+1} &= \mathbf{v}_i^{k+1/2} + \mu \mathbf{L}_i^{k+1/2} \end{aligned} \tag{3}$$

where the Laplacian is recalculated at each step. Here, $\mu = -\lambda$ is used and this is known as bi-Laplacian smoothing [26] and is analogous to the minimization of the thin plate energy of the surface [28].

The method employed for this study is based on the bi-Laplacian iterative method, using both isotropic and anisotropic schemes, defined by regions characterized by different curvatures. By first identifying the regions and then applying the process with different values of λ, tailored to each region, an accurate smoothing process is achieved. For the nasal cavity geometry, there are several high curvature regions, such as the olfactory cleft, which must be preserved, while spurious curvature variation due to the pixelated surface mesh needs to be removed. Furthermore, some low curvature regions are artefacts introduced due to uncertainty in segmentation, which is manifested as inter-slice rippling, and these also need to be removed.

DOI: 10.1002/fld

The smoothing process is divided into three steps. The reconstructed geometry is initially smoothed isotropically using 50 iterations of the bi-Laplacian scheme with $\lambda=0.6$. The second step is anisotropic smoothing, performed by carrying out 500 bi-Laplacian iterations with $\lambda=0.1$ for the higher curvature regions that include the medial passage and meatal crests, whereas for the rest of the geometry $\lambda=0.6$. The third phase to the smoothing is isotropic, performed using 200 bi-Laplacian iterations with $\lambda=0.6$. The appropriate re-inflation of the smoothed surface along its normal is performed iteratively at the end to minimize the distance between the geometries [1]. In the second smoothing step, in order to identify regions of higher curvature, the mean curvature at each node is calculated using the method proposed in [29] and is given by $\kappa_i = (1/4A_i)\sum_{j=1}^{m_i} \|(\cot(\alpha_j)+\cot(\beta_j))(\mathbf{v}_j-\mathbf{v}_i)\|$, where A_i is the area of the triangles surrounding node $\mathbf{v}_i$ and α_j and β_j are the angles opposite to side ij in the triangles sharing this side.

The original and smoothed geometries can be seen in Figure 4. The average absolute closest distance between the pixelated reconstruction and smoothed geometry is 0.19 pixels whereas the maximum is of the order of 1.5 pixels, for all three cases, occurring largely in the regions where the sinuses were artificially removed from the geometry. Over 99% of the smoothed geometry surface is below 0.5 pixels from the original reconstructed geometry. A number of schemes with

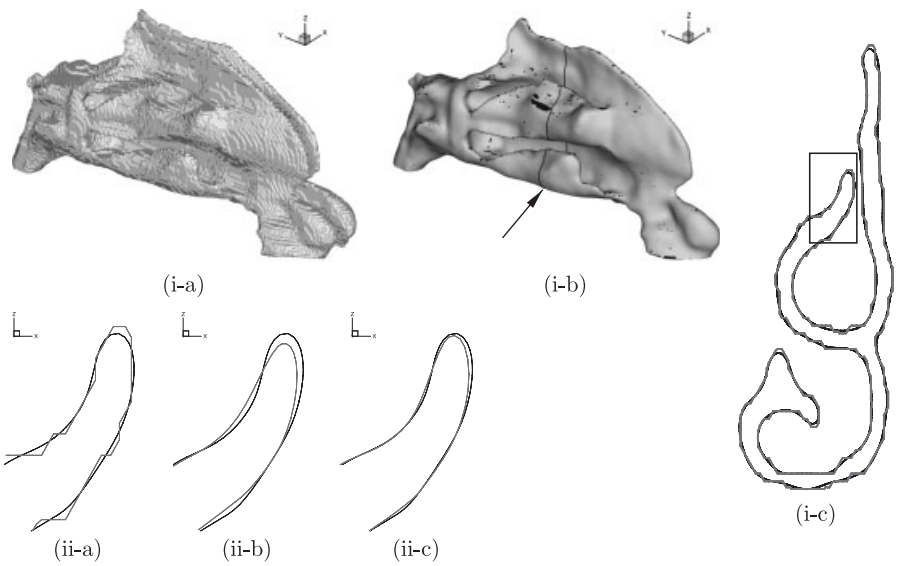

Figure 4. Smoothing procedure applied to Case 3, illustrating the change from the geometry after reconstruction (i-a) to the optimally smooth geometry (i-b). (i-b) Regions are shaded black if the absolute closest distance between the geometries is above 0.5 pixels (1 pixel = 0.39 mm). (i-c) Slice MC is shown, where the grey curve indicates the pixelated reconstructed surface and the black, the optimally smooth geometry. Details of the middle meatus crest of slice MC highlighting differences produced from different schemes are shown in (ii) where the black curve is the optimally smooth geometry and the grey curves indicate, respectively; (ii-a) the pixelated reconstructed geometry; (ii-b) application of 750 isotropic bi-Laplacian smoothing iterations; (ii-c) application of 250 isotropic bi-Laplacian smoothing iterations. Note that the smoothing schemes based solely on isotropic smoothing (ii-b) and (ii-c) perform worse by shrinking the geometry excessively than a mixed anisotropic approach.

DOI: 10.1002/fld

different parameters have been tested, with example shown in Figure 4, and the procedure outlined above was found to yield the best results.

For simplicity in the analysis, both visually and computationally, only the right nasal cavity is used in the remainder of this study. To be concise, the anatomically accurate smoothed geometries are referred to as *'true'* throughout the remainder of this paper.

3. SURFACE REPRESENTATION AS A STACK OF SLICES

Having obtained the anatomically accurate surface triangulation of the nasal cavity for the three cases, a compact representation that allows characterization and inter-patient comparison of morphologies is now developed. The method must be reversible such that the surface can be reconstructed without significant loss of information.

The approach proposed is based on considering the geometry surface in $\mathbb{R}^3$ as a stack of closed curves in $\mathbb{R}^2$. The number of slices extracted from the surface mesh should be sufficient to allow reconstruction of the surface from this stack, hence reversible. In this study, 50 equally spaced coronal slices are initially taken, as shown in Figure 5. The number of slices is based on the detail but has not been optimized; the choice represents, however, a good balance between computational cost and capturing the complex details sufficiently. The reconstruction of the surface from the slice stack is performed by using an implicit function formulation of the geometry surface and the interpolation of the closed curve stack by using RBFs.

The individual closed curves are characterized by using Fourier descriptors. These are the Fourier coefficients of a Fourier series expansion of a signal that represents the curve. The Fourier descriptors can be used to rebuild the cross-sectional closed curves, which are in turn sufficient to obtain once again the geometry surface.

By considering cross-sectional slices of the surface, the approach has several strengths: firstly, the amount of data to be processed at any time is less than considering the entire geometry; secondly, the Fourier descriptors from each slice are independent and can be analysed, compared and processed separately; thirdly, different regions of the topology may be studied individually.

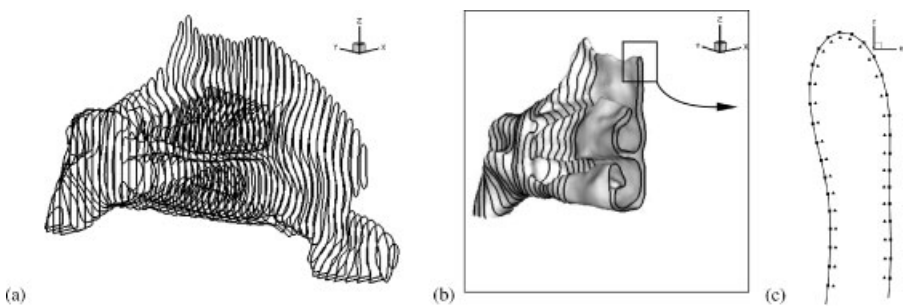

Figure 5. Patient Case 3: (a) 50 equally spaced closed contours in the coronal plane derived from the 'true' surface mesh. A continuous implicit function in 3D is fitted to these contours as shown in (b), with $f(x)=0$ on the contours and $f(x)=-1$ a short perpendicular distance inside the curves, a detail of which is shown in (c).

DOI: 10.1002/fld

The process of obtaining the surface from the slices via RBF interpolation is first discussed in Section 3.1 and Fourier descriptors are then described in Section 3.2.

3.1. Implicit function formulation

An implicit function formulation was used to reconstruct the right nasal cavity from the stack of 50 closed curves. The procedure for interpolating a surface through the contour stack is described in previous works [1, 30–32] and the discussion below is limited to a brief outline of the method. The difference between the 'true' topologies and those obtained by slicing the geometry and reconstructing it is within $\frac{1}{2}$ pixel on average (1 pixel = 0.39 mm). This shows that for the case studied, the 50 slices taken are sufficient to capture the topology in detail and to reconstruct the surface within an error of the same order of magnitude as the segmentation uncertainty.

Briefly, the surface interpolating between the boundary contours for each slice is defined as the zero-level iso-surface of an implicit function $f(x, y, z)$. Setting $f(x, y, z) = 0$ on equally sampled points of the cross-sectional stack defines the appropriately named *on-surface* constraints. A gradient is formed in the implicit function by introducing further constraints at a constant close distance normal to the curve, known as *off-surface* constraints, with $f(x, y, z) < -\alpha$ inside the curves and with $f(x, y, z) > \alpha$ outside the curves, where α is a positive constant. A regular spacing of constraints reduces the computational cost to solve the system in Equation (5) [33]. Typically, a larger number of on-surface constraints are used since these define the surface.

RBFs [31, 34, 35] are used to interpolate the constraints ensuring a unique solution. Consider a set of n constraints in $\mathbb{R}^3$ given by $\mathbf{x}_i = (x_i, y_i, z_i); i = 1, \ldots, n$ where each constraint has a value of h_i such that $f(\mathbf{x}_i) = h_i$; then for large n the implicit function can be expressed as

$$f(\mathbf{x}_i) = \sum_{j=1}^{n} \mathbf{c}_j \phi(\mathbf{x}_i - \mathbf{x}_j) \tag{4}$$

where $\phi(\mathbf{x}_i - \mathbf{x}_j)$ is the RBF and $\mathbf{c}_j$ is a set of coefficients. This can be expressed as a linear system of algebraic equations

$$\mathbf{h} = \mathbf{A}\,\mathbf{c} \tag{5}$$

where $\mathbf{A}_{ij} = \phi(\mathbf{x}_i - \mathbf{x}_j)$ is an $n \times n$ matrix. From [1, 31] the choice of the RBF is $\phi(\mathbf{x}_i - \mathbf{x}_j) = |\mathbf{x}_i - \mathbf{x}_j|^3$, where $|\cdot|$ denotes the Euclidean norm. The choice of RBF maps $\mathbb{R}^3 \to \mathbb{R}$ and $\mathbf{A}$ is non-singular and positive semi-definite. The linear system is solved using the generalized minimal residual method and the number of constraints typically used in this study is of the order of 35 000. Non-zero values introduced on the diagonal of $\mathbf{A}$ improve the computational time and is equivalent to approximating the implicit function to pass close to the constraints to produce a smooth interpolation in the presence of noise [32, 36]. Typical values for the diagonal terms of $\mathbf{A}$ are of the order of 10^{-3} pixels.

Having obtained the set of coefficients $\mathbf{c}_j$, the extraction of the zero-level iso-surface is accomplished by using the marching tetrahedral method, sampling the value of the implicit function at the vertices of a lattice of cubes containing the geometry, following [37], to obtain an initial triangulation.

3.2. Fourier descriptors

The method of Fourier descriptors is used to characterize the stack of closed curves. The airway boundary contour for each slice is first converted to a signal and the signal then expanded as a

DOI: 10.1002/fld

Fourier series. The coefficients in the Fourier expansion are termed the Fourier descriptors. For completeness the standard expressions for the Fourier expansion are included in the following summary of the method.

A closed curve $\gamma(l)$ can be expressed as a signal $g(l)$, where l is the perimeter length and $0 \leqslant l \leqslant L$, such that the signal has period L. A Fourier series expansion of g can be expressed as

$$\begin{aligned} g(l) &= \sum_{n=-\infty}^{\infty} c(n)\, \mathrm{e}^{\mathrm{i}nl} \\ c(n) &= \frac{1}{2L} \int_0^L g(l)\, \mathrm{e}^{-\mathrm{i}nl}\, \mathrm{d}l \end{aligned} \tag{6}$$

where $\mathrm{i} = \sqrt{-1}$. The discrete Fourier expansion is implemented for $g(l)$ by sampling at m equally spaced points to yield $g(k)$; $k = 0, \ldots, m-1$. The discrete Fourier transform (DFT) is given by

$$c(n) = \frac{1}{m} \sum_{k=0}^{m-1} g(k)\, \mathrm{e}^{-\mathrm{i}2\pi nk/m}, \quad 0 \leqslant n \leqslant m-1 \tag{7}$$

The real and complex components of $c(n)$ are the Fourier descriptors, denoted as $R(n)$ and $I(n)$, respectively. The amplitude, or energy, of the nth mode in the series expansion is given by $\sqrt{R(n)^2 + I(n)^2}$ and the phase of the nth mode is given by $\tan^{-1}(I(n)/R(n))$. To reconstruct $g(k)$ the inverse DFT (IDFT) is used, which is given by

$$g(k) = \sum_{n=0}^{m-1} c(n)\, \mathrm{e}^{\mathrm{i}2\pi nk/m}, \quad 0 \leqslant k \leqslant m-1 \tag{8}$$

Aliasing is avoided by ensuring that the cross-sectional contours are sufficiently well sampled and the higher-frequency modal components are of negligible amplitude.

By applying the DFT the Fourier descriptors that represent the contour curve γ are obtained and shape characterization may be performed by observing the energies in the modes. Furthermore, the signal g representing γ can be first manipulated, for example, by filtering the signal to keep the dominant modes only, and γ then reconstructed using the IDFT.

Signals $g(l)$ of closed curve $\gamma(l)$ may be formulated by considering either the change in angular direction [16] or Cartesian coordinates [17, 19, 38, 39]. The relative advantages and limitations of both respective representations merit some consideration as follows.

First, a contour in $\mathbb{R}^2$ may be defined in terms of the normalized cumulative angular change of a point moving along the perimeter [16]. Denote the angular direction of γ at a location l by $\theta(l)$ and define the cumulative angular function $\phi(l)$ as the net angular bend between $\theta(0)$ and $\theta(l)$. With the anticlockwise convention, moving in this direction around γ results in $\phi(L) = \phi(0) + 2\pi$; hence, the signal is not periodic. Let us define $\phi^*(t) = \phi(Lt/2\pi) - t$ as the normalized cumulative angular function where $\phi^*(0) = \phi^*(L) = 0$ and $t = 2\pi l/L$. Signal $\phi^*(t)$ is invariant under translation, rotation and scaling and has period 2π. For a circle, $\phi^*(t) = 0$ and hence the normalized cumulative angular function can be seen as a deviation from a circle. In Figure 6, signal $\phi^*(l)$ for slice middle cavity (MC) of subject Case 3, illustrated in Figure 2, is shown. From this, features corresponding to the surface may be identified, as well as the size of the feature details from the amplitude of the oscillations in the signal.

Applying the Fourier transform to $g(l) = \phi^*(t)$ allows for the characterization of the curve by obtaining the coefficients; however, this approach suffers from non-closure of the curve if it is

DOI: 10.1002/fld

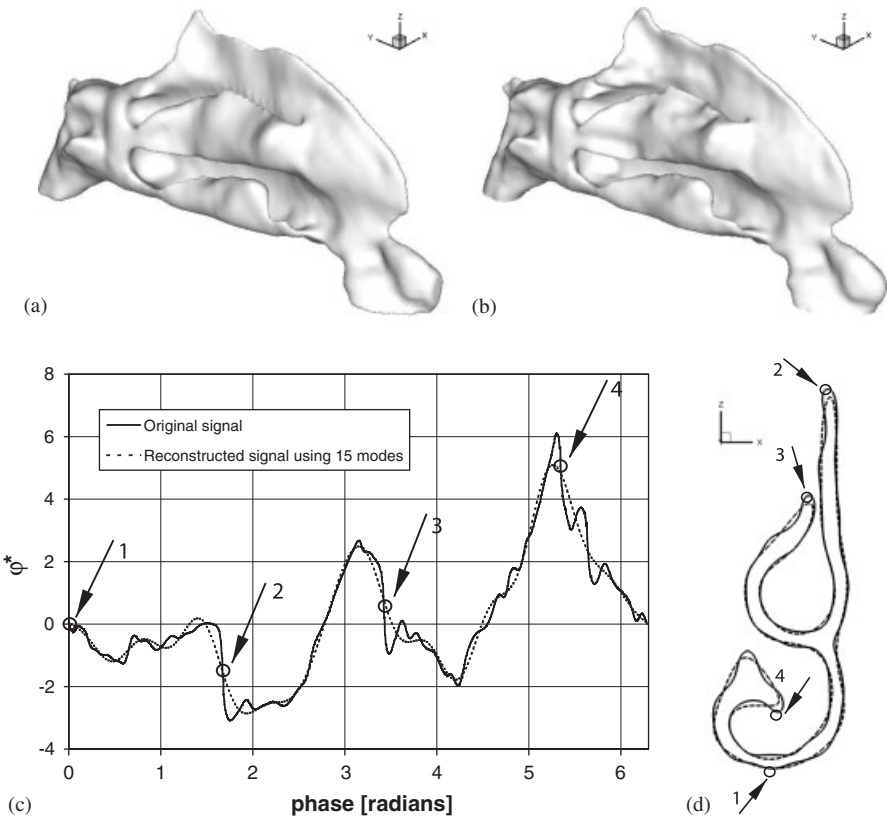

Figure 6. The reduced geometry of Case 3 reconstructed with 15 Fourier modes (a, reduced geometry) is noticeably smoother than the 'true' geometry (b, 'true' geometry) while still preserving the topology. Signal ϕ^* (c) of slice MC (d) for both the original (solid line) and reduced (dashed line) signals. Closest distance maps for these geometries are shown in Figure 9.

reconstructed using anything but the full set of coefficients [16]. This is because the reconstruction of $\gamma(l)$ from $\phi^*(l)$ is cumulative and hence dependent on the previous position and tangent. Although the approach is good at describing γ with few dominant modes and signal $\phi^*(l)$ easily physically interpretable, it is inadequate in the work proposed here since it does not allow reconstruction of γ from a filtered series expansion of ϕ^*.

The second method to describe a curve, now implementable also in $\mathbb{R}^3$, is based on the change of the Cartesian coordinates of the curve as a function of l. The signal that describes the curve is given by $g(l) = \mathbf{x}^*(l) = (x(l) - x(0), y(l) - y(0), z(l) - z(0))$ and hence a signal for each axis. This approach is more costly since it requires more functions to describe γ; however, it can be used to describe curves in 3D and is free from the limitation of non-closure if the curve is reconstructed from a filtered series.

In Figure 7 the amplitude of the first mode of signal $\mathbf{x}^*(l)$ is shown, for the equally spaced cross-sectional stack for Case 3 as well as for the first 50 modes for slice MC (number 25 in the stack). The first Fourier mode is equivalent to an ellipse and the energy carried by the first mode

DOI: 10.1002/fld

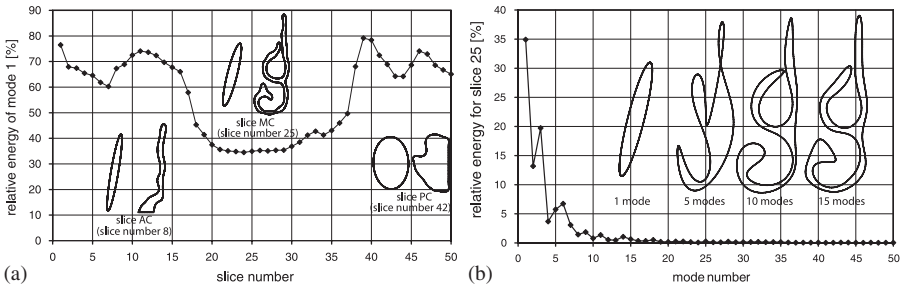

Figure 7. Relative energy of the Fourier modes of signal $\mathbf{x}^*(l)$, given as percentage of the sum of all the modes. The cross-sectional stack is equally spaced and belonging to Case 3. (a) The energy of the first mode along the stack and (b) the energy for the first 50 modes in slice MC.

with respect to the energy of the full set of modes is a measure of the ellipticity of the cross section. Even for slice MC, which has low ellipticity, it is evident that the dominant modes are those with lowest frequency, with the energy quickly decreasing for higher modes. A low-pass filter will hence retain the dominant modes. A simple truncation of the series is equivalent to a crude low-pass filter and has been used for simplicity in this study, although a properly shaped low-pass filter would likely prove superior.

Using this information, the signals of the stack of slices belonging to Case 3 have been reduced, or simplified, by low-pass filtering, with no compensation for the energy removed. The resultant geometry and the signal $\phi^*(l)$ for slice MC are shown in Figure 6. The 'true' and reduced geometries appear to be very similar topologically, indicating that the dominant Fourier modes ($\sim$95% or more of the energy) can describe the geometry sufficiently; however, it is also necessary to study the fluid behaviour since it concerns the function of the nasal passage. If the flow field in both the reduced and 'true' geometries are similar, then the dominant modes in the Fourier series can in fact represent and characterize the necessary boundary definitions to determine the flow.

4. COMPARISON OF FLOW IN REDUCED AND 'TRUE' GEOMETRIES

Computations of steady, inspiratory flow were performed for both the 'true' geometry and that derived by retaining only the first 15 Fourier descriptors in the slice definition (50 equally spaced slices) for Case 3. The reduced geometry thus constitutes a crude low-pass filtering of the slice modal expansion that retains approximately 95% of the total energy in the modal decomposition. To quantify the effect of geometry simplification on the flow, and to relate changes in geometry and flow, local and global measures are used.

The local topological differences between 'true' and reduced geometries are obtained by determining the closest distance between the geometry surfaces, whereas the wetted surface and volume changes represent global differences. The measures used in studying the flow field differences are based on the WSS, particle tracks, clearance times, pressure drop and cross sections of the velocity at slices AC, MC and posterior cavity (PC). Together these provide a sensitive means of identifying and quantifying the geometry and flow field changes.

DOI: 10.1002/fld

4.1. *Flow conditions and methodology*

The inflow boundary condition is taken to be a blunt velocity profile with a volume flux of 100 ml/s (1.01 m/s inflow velocity at the naris); $Re \approx 900$ based on the hydraulic diameter of the nasal valve. This is low enough for the flow to be laminar, as discussed in [40], and verified for this model by *in vitro* experiment using an anatomically accurate replica [41]. This volume flux of 12 l/min (6 l/min through each nostril) is equivalent to quiet restful breathing [4, 42]. At a flow rate of 115 ml/s, slightly above that chosen, the first evidence of unsteadiness appears for this geometry, as demonstrated by experimental studies, [41], where also the effects of higher flow rates (170 ml/s) on transport are revealed by dye visualization. In general, higher flow rates appear to lead to disturbed laminar flows, in which complex interactions between the flow instability and the geometry greatly alter dispersion.

The numerical schemes are based on finite volume solutions of the steady incompressible, Newtonian, Navier–Stokes equations using Fluent 6.2.16 [43]. The pressure was solved using a second-order accurate scheme, the pressure–velocity is coupled using the SIMPLE method and the momentum is approximated using a third-order upwind scheme. The segregated approach to solving the algebraic equations of continuity and momentum is used.

The volume mesh is generated using TGrid [44] to yield four prismatic elements across the boundary layer and an unstructured tetrahedral mesh core containing 8 million cells. A cross section of the reduced geometry mesh is shown in Figure 8. The height of the prismatic elements nearest to the wall is 3.5×10^{-5} m corresponding to the order of 1% of a characteristic nasal valve radius. Mesh convergence is assured by following the work presented in [45] where for the same patient case, the mean local error in WSS (mean measure of the difference in WSS at a point) between a 3.5 million cell mesh and a 15 million cell mesh is approximately 8%.

Approximately 40 000 equi-spaced massless particles were introduced at the naris, where a uniform inflow was prescribed, and their pathlines computed using an in-house code employing a second-order spatial and temporal integration. Spatial and temporal convergences were determined

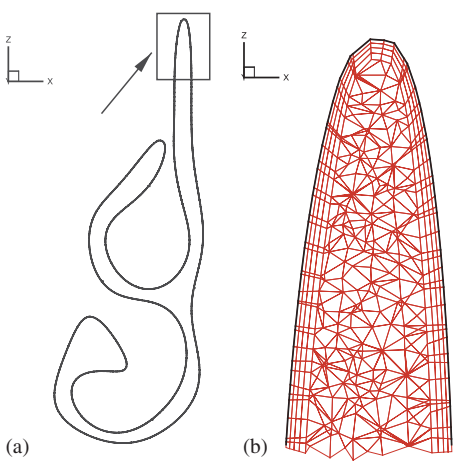

Figure 8. (a) Coronal cross section (slice MC) of the right nasal cavity of the reduced geometry and (b) detail of the medial passage crest.

DOI: 10.1002/fld

using grid refinement and variable time step, respectively. The cumulative error on integration in tracking particles between inlet and outlet is found to be of the order of 5×10^{-6} m difference at end location, for the nasal cavity geometry, when halving the integration time step used. Normalizing the error to the diameter of the naris inflow, the error is of the order of 0.1%.

4.2. Effects of surface simplification on the geometry

The closest distance between the 'true' and reduced geometries is shown in Figure 9, where the distance is normalized to a pixel. It is clear that the largest portion of the difference in the geometry surfaces occurs in horizontal strips of small-scale oscillations in the middle cavity region. As shown in Figure 6, low-pass filtering the Fourier series has a smoothing effect, removing high-frequency oscillations present in the 'true' geometry, which are caused by local topological features.

The majority of the difference in geometries occurs in the middle cavity region since the energy of the 15 modes used to reconstruct the reduced geometry captures a lower portion of the total signal energy with respect to other regions, as discussed later. This is partly due to small-scale oscillations that occur in the 'true' geometry that have a wavelength of a couple of pixels (shown in Figure 6(c)), corresponding to a higher frequency in the middle cavity region due to the greater perimeter length compared with the anterior or posterior regions. A low-pass filter admits adequate spectral components in the anterior and posterior regions but less so in the middle cavity region.

The largest change is seen in the crests of the medial passage and meatuses, which are given in part by the higher Fourier modes that have been filtered. The mean absolute closest distance is 25% of a pixel width, whereas the maximum value is found to be in the medial passage crest and is 2 pixels.

The surface area and the volume, shown further on in Table I, are greater for the 'true' geometry, but these differences are only 4.1 and 1.5%, respectively.

Inter-individual and intra-individual (including due to the nasal cycle) variabilities in the morphology are noticeably greater than those obtained between the 'true' and reduced models [4, 8]. This is also seen later in Section 5 where three different patient morphologies are compared.

4.3. Effects of surface simplification on the flow

Comparison of the velocity field in the 'true' and reduced models is shown in Figure 10 for three slices, AC, MC and PC, the locations of which are marked in Figure 2. As flow traverses the cavity, the range of velocities diminishes, though there remains considerable spatial variation in magnitude.

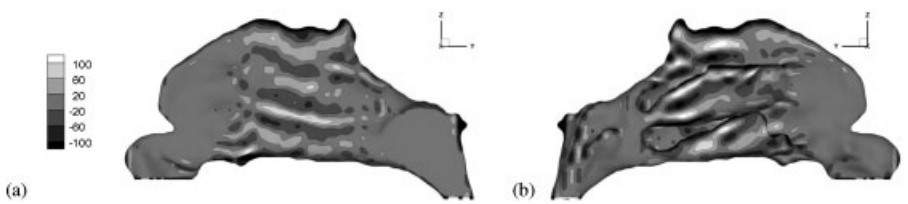

Figure 9. 'True' geometry with closest distance map between the 'true' and reduced geometries, given as percentage pixel. Views in the sagittal plane from (a) the septum and (b) the turbinates sides.

DOI: 10.1002/fld

Table I. Results for Case 3 true geometry and its simplification by using of 15 Fourier modes.

	True	Reduced
Mean wall shear stress (Pa)	0.059	0.060
Mean wall shear stress in olfactory cleft region (Pa)	0.031	0.032
Mean wall shear stress in middle turbinate anterior head (Pa)	0.170	0.180
Number of particles traversing olfactory cleft (%)	9.0	10.2
Pressure drop across geometry (Pa)	9.8	9.8
(Pressure drop/dynamic head) at slice AC	0.005	0.005
(Pressure drop/dynamic head) at slice MC	0.021	0.020
(Pressure drop/dynamic head) at slice PC	0.039	0.039
Surface area (cm^2)	106.26	101.92
Volume (cm^3)	13.83	13.62

The region taken for the olfactory cleft is indicated in Figure 13.

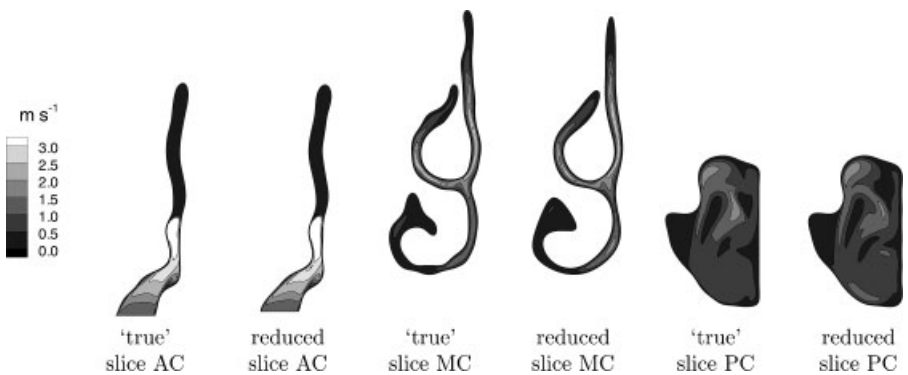

Figure 10. Comparison of velocity magnitude cross sections, as shown in Figure 2. The cross sections result shifted vertically to indicate their relative positions in the geometry.

Slice AC shows the strong inspiratory jet of air funnelled into the main cavity from the nasal vestibule. The upper margin of the jet adjoins a large region of low velocity flow in the anterior part of the cavity, shown in the following section to comprise a zone of flow recirculation. The jet appears slightly broader in the reduced model than in 'true' geometry. The inspiratory peak velocity is 3.7 and 3.8 m/s for the 'true' and reduced geometries, respectively, and are located in slice AC. These peak velocities are comparable to those found in previous studies using different nasal cavity models [4, 14, 46, 47].

Slice MC demonstrates that the majority of the flow is directed about the lower margins of the middle turbinate and the septal side of the inferior turbinate in both 'true' and reduced models, with scarcely any flow in the upper reaches of the inferior meatus. Both models indicate low flow to the olfactory cleft, though a slight increase is apparent for the reduced model. Although the greatest portion of the noticeable change in the velocity occurs in the crests of the meatuses and medial passage, these regions contain slow moving flow with small volume flux ($\sim$10% in the olfactory cleft as delineated in Figure 13, as similarly documented in [4, 40, 46]) and do not significantly

DOI: 10.1002/fld

influence the bulk convective transport through the cavity. Slice PC shows very similar details for the flow passing to the nasopharynx in both models.

The Lagrangian pathlines followed by massless point particles traversing the cavity not only reveal dominant features in the flow but also provide information on the degree of mixing, partitioning and retention of the flow in different functional zones. The tracks of such particles as they convect from the naris inlet to the nasopharynx outlet are shown in Figure 11 for the 'true' geometry only, as the results are very similar for both 'true' and reduced models. Although massless particle tracks provide useful information regarding the flow, they do not provide information on realistic particles and deposition. They are, however, more sensitive in highlighting differences between the flow in different models since they are affected neither by inertia (significant for larger particles) nor diffusion (significant for nanoscale species), and are used for this purpose here.

The pathlines clearly indicate the large recirculation zone in the anterior part of the cavity. The re-attachment region on the crest of the medial passage occurs towards the start of the olfactory region and the re-attachment point was found to be only 0.8 mm apart on the medial passage crest between the 'true' and reduced geometries.

The inspiratory jet is seen in Figure 11 to be directed predominantly onto the middle turbinate but also passes by the septal-facing side of the inferior turbinate and along the medial passage. The impingement of the flow on the middle turbinate causes the flow to be redirected partly in the middle meatus and partly in the upper portion of the medial passage, dictating the reattachment location of the recirculating flow located above the nasal valve. Twisting of the pathlines entering the main cavity indicates the presence of streamwise vortical structures.

In Figure 11 the clearance times are also presented, defined as the time taken for a particle to clear the domain from the naris inlet to the nasopharynx outlet, and presented here as a frequency distribution. For reduced geometry, there is a slight lag for the initial particle exit time and a sharper decrease in number of particles for the longer times. The mean clearance time, however, is the same for both geometries at 0.13 s.

The location of particles as they cross slice MC are compared for the two models in Figure 12, where two different particle origin labelling schemes are employed to illustrate the degree of convective mixing (strictly 'stirring' rather than mixing since diffusion is neglected). Although some slight differences can be discerned, the close similarity between the overall particle distributions is

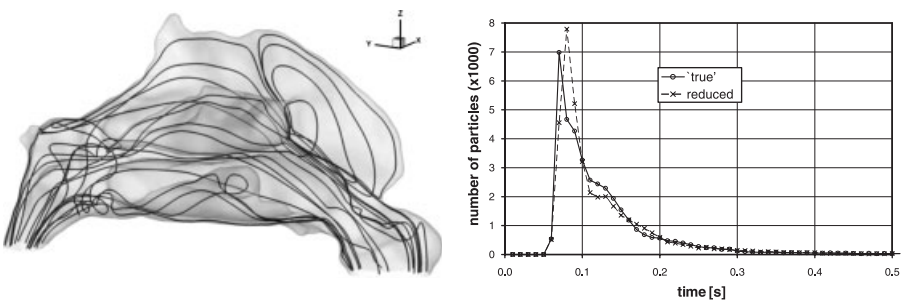

Figure 11. Illustrative particle tracks in the 'true' geometry and the clearance times frequency distribution for $O(40000)$ particles, given as the time to traverse the domain from inlet to outlet. Mean clearance time $= 0.13$ s for both the 'true' and reduced geometries.

DOI: 10.1002/fld

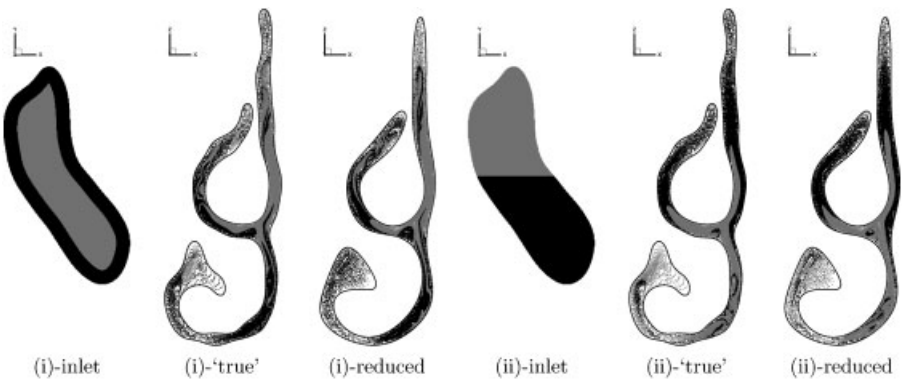

Figure 12. Particle track section at slice MC for 'true' and reduced geometries. The particle tracks are shaded by their seeding location at the naris inlet and based on the distance from the geometry wall for (i) and in the front-back direction in (ii). The number of particles in both species is the same and a total number $O(40000)$.

evident. Overall, the coherence of the labelling at slice MC indicates that the degree of flow mixing is relatively low. From the functional perspective, it is particularly interesting that the particles entering the olfactory cleft are labelled as originating from the forward part of the naris (dark shading in Figure 12(ii)).

By mapping the WSS of the reduced onto the 'true' geometry, based on a closest distance correspondence [1], the local change in the WSS in Pa and a percentage change, normalized to the local value, are obtained and shown in Figure 13. Comparing these results with those shown in Figure 9 illustrates the non-local dependence of flow on geometry. Fine differences in WSS distribution are revealed in the olfactory cleft, which is a region of low WSS, at the margins of the jet, and its impact on the middle turbinate. Again, the particular sensitivity of flow in regions of constriction, such as the nasal valve, is highlighted by the plots.

Indeed, closer study of the nasal valve cross section shown in Figure 14 indicates a small change in the shape towards the upper portion, which is the likely source of much of the change in WSS patterns.

Although the percentage change in WSS can be very large in localized regions, the average WSS is 5.9×10^{-2} and 6.0×10^{-2} Pa for the 'true' and reduced geometries, respectively, which reflects the lack of change in the pressure loss across the cavity. Furthermore, the standard deviation of the local WSS difference between the 'true' and reduced models is 2.6×10^{-2} Pa, indicating also small localized spatial differences in WSS. If we consider sensitive regions of relevance to nasal physiology such as the anterior head of the middle turbinate (shown in Figure 15) for deposition and the olfactory region for the sense of smell, we note that the average differences in WSS between the 'true' and redundant geometries in these regions are 0.01 and 0.001 Pa, respectively. These differences indicate small regional changes in WSS, which will likely not alter significantly nasal functionality and nasal sensation.

An important and sensitive region is the anterior head of the middle turbinate [48] where the vortical structure and the jet from the nasal valve impinge, resulting in a complex flow pattern forming, including the shedding of a pair on counter-rotating vortices being shed and running along the middle turbinate tip. On comparing the WSS magnitude and the surface shear lines,

DOI: 10.1002/fld

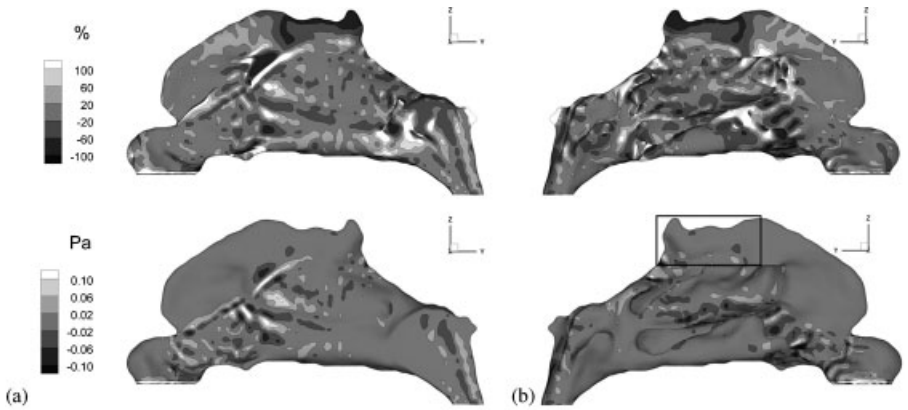

Figure 13. Difference in wall shear stress between 'true' and reduced geometries, presented as local change (%) and absolute change (Pa). The rectangle in the lower right image delineates the approximate olfactory cleft region, used to determine average olfactory wall shear stress and fractional particle flux. Views in the sagittal plane from (a) the septum and (b) the turbinates sides.

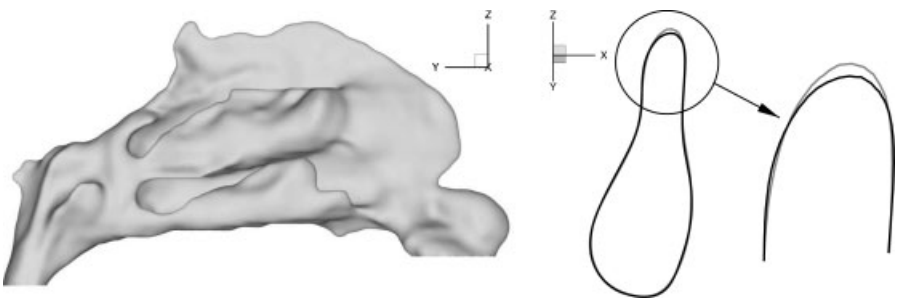

Figure 14. Cross section of the nasal valve. The black cross section belongs to 'true' geometry and the grey belongs to reduced geometry.

which are aligned with the tangential component of the viscous traction exerted by the flow on the wall, for both 'true' and reduced models, shown in Figure 15, we see that there is a localized change in the WSS; however, the stagnation point has moved by only 0.5 mm.

Summary of comparison of the geometry and flow in 'true' and reduced models is contained in Table I. Integrated measures such as surface area, volume, pressure, wall shear show close correspondence. The reduced model is biased by shrinkage induced in the uncompensated filtering by truncation of the geometric modal expansion, though only slightly, and this has not been corrected for. Although large variations in point-wise samples of wall shear were found, the changes, once integrated even over a restricted functional region, such as the olfactory cleft, are small and unlikely to affect physiological performance. The slight increase in WSS and particles directed to the olfactory cleft observed for the reduced model is consistent with improved flow through a slightly less tortuous passage. Overall, it can be concluded therefore that the reduced model provides a flow field closely matching that of the original 'true' geometry.

DOI: 10.1002/fld

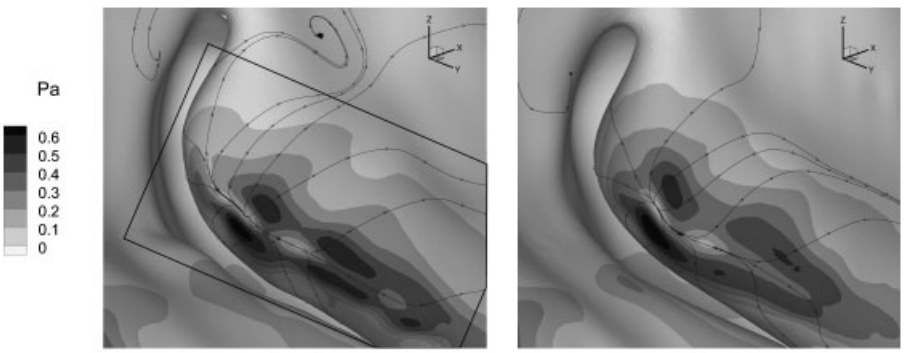

Figure 15. Detailed view of the middle turbinate from inside the domain for 'true' and reduced geometries. Although the spatial distributions of WSS magnitude in this sensitive location are seen to change slightly, patterns of surface shear lines show comparable flow structure and stagnation location. The rectangle shown in the left figure indicates the extent of zone on anterior head of middle turbinate used to compare mean regional WSS averages.

5. INTER-PATIENT OBSERVATIONS USING FOURIER DESCRIPTORS

Up to now, only the geometry of subject Case 3 has been used in the Fourier descriptor and CFD analysis to show that the dominant modes in the Fourier series can contain the information to describe the geometry and preserve features of the flow field. Two further nasal airway geometries, shown in Figure 16, are used to investigate the use of the Fourier descriptors to characterize and discriminate between topologies.

Observing again the energy variation of the first Fourier mode of signal $\mathbf{x}^*(l)$ along the stack for Case 3, shown in Figure 7, the elongated form of the cross sections and the different features in the topology noticeably affect the energy distribution across modes. For example, referring to Figure 7(a), an increase in the first (simple elliptical mode) energy from slice 7 to slice 8 occurs at the end of the naris inlet; the start of the inferior meatus produces an initial decrease in mode 1 contribution at slice 14; the start of the middle meatus greatly reduces the resemblance of the boundary to a simple ellipse, with a noticeable decrease at slice 17; whereas the end of the meatal passages and the start of the nasopharynx is marked by the increased weight given to mode 1 around slice 38.

In a similar approach, Fourier descriptor decomposition has been performed on the three patient cases, identifying the start and end of the middle meatus as shown in Figure 16. It is important to note that to allow for the slicing of the geometries of the cases, it is first necessary to register the surfaces to obtain a common pose. This was performed using the iterative closest point method described in [24, 49, 50].

To analyse and compare the topologies, the surface is sliced with respect to the three different regions: anterior, middle and posterior, as given by the middle meatus start and end location landmarks. Furthermore, due to the different complexities of the three regions, 10 equally spaced slices in the anterior and posterior regions and 30 equally spaced slices in the middle region have been taken. Therefore, slices 1–10 correspond to the anterior region, 11–40 to the middle region and 41–50 to the posterior region. Since these slices are corresponding based on the landmark

DOI: 10.1002/fld

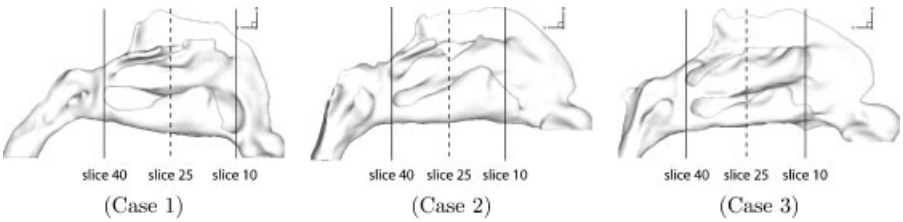

Figure 16. Sagittal views of three patient cases with the start and end of the middle meatus in the coronal plane identified by the solid line. The airway is therefore divided into three regions: anterior, middle and posterior cavities, based on the location of the start and end of the middle meatus landmarks. The dashed line indicates the location of slice 25 in the stack, shown in the coronal plane in Figure 17.

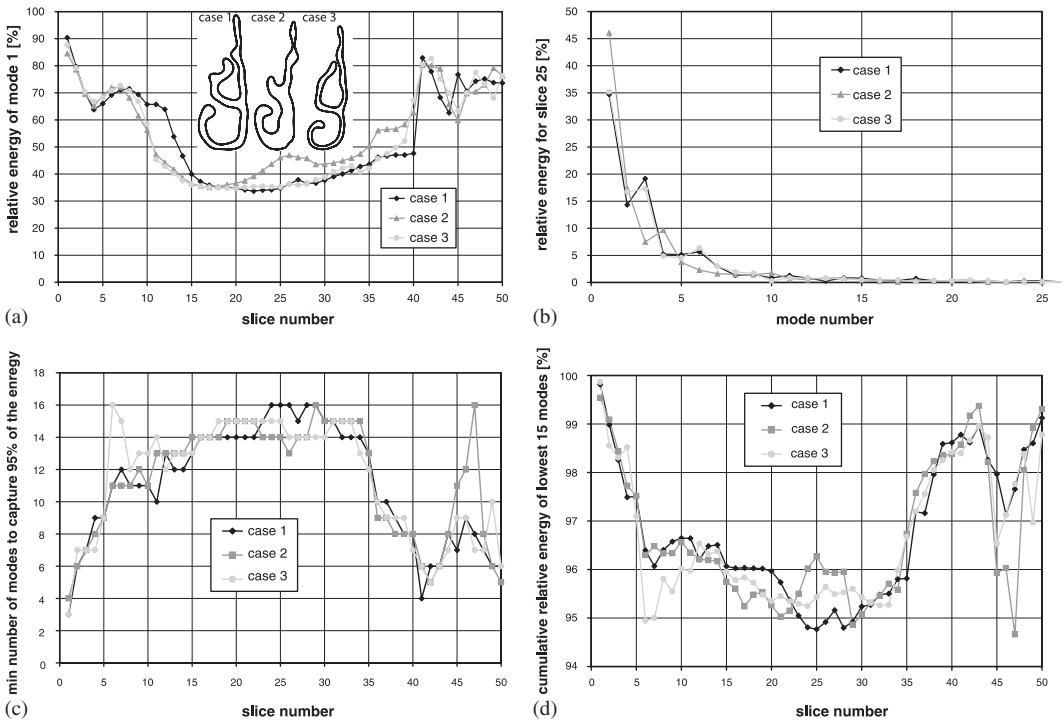

Figure 17. Relative energy of the Fourier modes of signal $\mathbf{x}^*(l)$, given as percentage of the sum of all the modes. The cross-sectional stack is equally spaced in the three regions given by the anterior, middle and posterior portions of the airway (shown in Figure 16); with 10, 30 and 10 slices in each region, respectively. (a) The energy of the first mode along the stack; (b) the energy for the first 25 modes in slice 25; (c) the minimum number of modes required to capture at least 95% of the signal energy; and (d) the percentage energy captured by the first 15 modes for all the cross sections.

DOI: 10.1002/fld

feature of the middle meatus start and end locations, direct inter-patient comparison of the energies of the modes can be performed. The number of slices is taken to be indicative of the variations in signal that may be observed but has not been optimized.

The energy variation of the first Fourier mode of signal $\mathbf{x}^*(l)$ along the stack and the energy for the first 25 modes for slice 25 are shown in Figure 17 for the three cases. Although the energy spectrum is similar, marked differences occur firstly in slices 10–15 for Case 1 (due to the lower meatus starting at a later slice in Case 1 compared with Cases 2 and 3) and secondly in slices 20–30 for Case 2 (due to a greater width of passage and reduced size of middle meatus of Case 2 compared with Cases 1 and 3).

As shown in Figure 17, it is evident from the energy of the first 25 modes of slice 25 (low elipticity) for all cases that the dominant modes belong to the lower frequencies, rapidly decreasing in the energy they carry for higher frequencies. In fact for the cross-sectional stack of each case, the cumulative relative energy of the first 15 modes contains approximately 95% or more of the energy. Although in this work the lowest 15 modes have been taken for each cross section, a reduced set of modes could have been chosen by selecting only the necessary number of dominant modes to achieve a cumulative relative energy of 95%.

Since the surface slicing is based on the landmark features of the middle meatus start and end locations, the slices are corresponding. Direct comparison of the energy carried by each mode for a corresponding slice is possible, resulting in a measure of relative geometric deviation energy of a case from another. In this manner, geometries may be characterized.

6. CONCLUSION

It has been shown that a compact, hierarchical and reversible representation of the complex biological conduit geometry of the human nasal airways is achievable. This study describes an approach to study and to characterize complex geometry with a filtered data set that preserves the gross flow features; the techniques are versatile, readily implementable and may be further refined. The methodology proposed offers a means to investigate variations in conduit morphology and their effects on the computed flow in a rational and systematic way.

To summarize the findings, firstly, methods to derive the cavity wall boundary from medical images have been outlined, including medical image segmentation and anisotropic smoothing of the boundary surface, which provide less geometric distortion in regions of high curvature such as in the olfactory cleft. Secondly, the use of both Fourier descriptors and RBF interpolation to perform a patient-specific study of inspired flow for restful breathing was outlined. Computational modelling of inspiratory flow was used to derive values of sensitive parameters, relevant for physiological modelling. The data complements those of other investigations, e.g. [4, 15, 40, 46, 51], but few other nasal airflow studies have previously considered the sensitivity of flow in a patient-specific model to small perturbations in boundary geometry. Thirdly, application of the methods to compare the geometry of different subjects was outlined, and inter-individual morphology comparison was shown to be feasible using the methods discussed.

More specifically, the methodology and findings are as follows. The feasibility of compressing data by describing the necessary geometry surface boundary definitions to determine the flow as a set of dominant Fourier descriptors has been shown. The slice-based Fourier descriptor expansion coupled with the implicit function surface interpolation provides a reversible, hierarchical and compact representation of the geometry. The Fourier descriptors can hence be applied to

DOI: 10.1002/fld

characterize and to decompose the geometry. In particular, low-pass filtering the Fourier series to retain the dominant modes may be used to reduce the information and hence complexity of the geometry.

Computations of the steady inspiratory flow in the 'true' and a slightly reduced geometry illustrated the key features of nasal airflow, with Lagrangian particle tracking used to determine the residence time distribution of flow particles in the cavity. Comparison of the results for both models revealed that a compact representation of the geometry (retaining approximately 95% or more of the relative signal energy in just 15 modes), preserved highly sensitive local features such as the reattachment point in the olfactory cleft, as well as regionally averaged WSS and particle flux.

The main finding of physiological relevance was that, for the subject nose considered, although the relatively minor geometrical perturbations introduced by boundary approximation induced significant point-wise variations in sensitive measures such as WSS, regionally averaged measures showed little variation. Specifically, the WSS and percentage flux of marker particles in the olfactory cleft, and the mean WSS imposed on the anterior head of the middle turbinate, were not significantly altered. Given that there is always some degree of uncertainty in image segmentation parameters such as the threshold level, it is encouraging that minor perturbations did not grossly alter functional assessment of nasal airway performance in this case. Caution is needed before attempting to generalize this finding—changes to a critical, flow-limiting region such as the internal nasal valve can significantly alter cavity flow [4], but in this case the nasal valve geometry was barely altered (cf. Figure 14).

A brief outline of the use of Fourier descriptors to compare different subject anatomies was described. It was shown that by observing the energies carried by the lowest Fourier modes, landmark features can be identified and inter-patient comparison rendered possible due to the direct correspondence of the cross sections, and hence corresponding Fourier descriptors. The relative energies of the modes for corresponding slices provides a measure of the deviation from one geometry surface to another.

Although these procedures have been implemented for the nasal cavity geometry, the methods described are versatile and could be implemented for other geometries to characterize the morphology and flow field. Other developments of the methods are possible, for example, averaging and morphing between geometries using weighted averages of the Fourier descriptors, or the use of Fourier descriptors directly in the segmentation process.

Other experimental work [51] considered different small variations in model geometry originating from variations in the image segmentation choices made by different operators, current CT image resolution being insufficient to permit unambiguous airway delineation everywhere in the cavity. However, experiment does not permit such detailed quantification of flow. The geometric reduction technique may be used therefore not only as a means of providing a compact representation, suitable for comparison but also as a means of investigating geometric sensitivity for a given model. More drastic pruning of the modal expansion may be used as a form of geometry idealization, and flow sensitivity to more gross changes investigated.

This work has focused on the methodology of the morphological characterization. Although laminar restful breathing has been used here and verified for this model by *in vitro* experiment using an accurate replica [51], a greater spectrum of flow boundary conditions remains necessary in studying the link between form and function of the nasal cavity. This, however, remains beyond the scope of this work; current numerical modelling for turbulent flows [52, 53] does not attempt to represent the laminar-transitional phenomena known to occur and observed in recent time-resolved experiments [41].

DOI: 10.1002/fld

Since results of the CFD analysis have shown that the reduced geometry formed using the dominant Fourier descriptors performs very similarly to the 'true' one, a future study of the dominant Fourier descriptors from a larger population may feasibly aid in classifying characteristic flow patterns associated with morphological modes. This could be developed further as an essential component in patient-specific prognosis for clinical application.

Although it has been shown that the dominant modes may characterize the geometries, an in-depth analysis of the deviations of all the modes has not been attempted in this study, which is directed towards introducing the concept and feasibility of the method. Other factors such as the optimal number of slices to be taken and the preferred slicing planes are also deferred to future studies, for which a greater population of patient data is required.

NOMENCLATURE

$\mathbf{v}_i$	mesh vertices
$\mathbf{L}_i$	discrete Laplacian at vertex i
m_i	number of neighbouring vertices to vertex i
ω_{ij}	weight to calculate the discrete Laplacian
λ, μ	shrinkage and inflation weights to the smoothing
κ_i	mean curvature at vertex i
A_i	area of triangles surrounding vertex i
α_j, β_j	angles opposite side ij in the triangles sharing this side
$f(\mathbf{x}_i)$	implicit function
$\mathbf{c}_j$	coefficients in the implicit function formulation
$\phi(\mathbf{x}_i - \mathbf{x}_j)$	radial basis function
$\gamma(l)$	closed curve
$g(l)$	periodic signal representing the closed curve $\gamma(l)$
l	perimeter length
$c(n)$	Fourier series expansion coefficients
$\phi^*(l)$	normalized cumulative angular function as $g(l)$
$\mathbf{x}^*(l)$	change along Cartesian axes function as $g(l)$

ACKNOWLEDGEMENTS

The authors are grateful for the support of the Biotechnology and Biological Sciences Research Council (BBSRC) who funded much of this research, under grant programmes E18557 and BB/E02344/1, and to the HPCx National Computing Resource for additional support. We are grateful for the assistance in model segmentation of Dr R. Almeyda, formerly of the ENT Department of St Mary's Hospital in Paddington.

REFERENCES

1. Gambaruto AM, Peiró J, Doorly DJ, Radaelli A. Reconstruction of shape and its effect on flow in arterial conduits. *International Journal for Numerical Methods in Fluids* 2008; **57**(5):495–517.
2. Wolf M, Naftali S, Schroter RC, Elad D. Air-conditioning characteristics of the human nose. *The Journal of Laryngology and Otology* 2004; **118**:87–92.
3. Mygind N, Dahl R. Anatomy, physiology and function of the nasal cavities in health and disease. *Advanced Drug Delivery Reviews* 1998; **29**:3–11.

DOI: 10.1002/fld

4. Zhao K, Scherer PW, Hajiloo SA, Dalton P. Effect of anatomy on human nasal air flow and odorant transport patterns: implications for olfaction. *Journal of Controlled Release* 2004; **29**:365–379.
5. Illum L. Nasal drug delivery possibilities, problems and solutions. *Journal of Controlled Release* 2003; **87**: 187–198.
6. Kleven M, Melaaen MC, Reimers M, Rotnes JS, Aurdal L, Djupesland PG. Using computational fluid dynamics (CFD) to improve the bi-directional nasal drug delivery concept. *Food and Bioproducts Processing* 2005; **83**(C2):107–117.
7. Schroeter JD, Kimbell JS, Asgharian B. Analysis of particle deposition in the turbinate and olfactory regions using a human nasal computational fluid dynamic model. *Journal of Aerosol Medicine* 2006; **19**:301–313.
8. Churchill SE, Shacklford LL, Georgi JN, Black MT. Morphological variation and airflow dynamics in the human nose. *American Journal of Human Biology* 2004; **16**:625–638.
9. Franciscus RG, Long JC. Variation in human nasal height and breadth. *American Journal of Physical Anthropology* 1991; **85**:419–427.
10. Cakmak O, Coskun M, Celik H, Buyuklu F, Ozluoglu LN. The value of acoustic rhinometry for measuring nasal valve area. *The Laryngoscope* 2003; **113**:295–302.
11. Schreck S, Sullivan KJ, Ho CM, Chang HK. Correlations between flow resistance and geometry in a model of the human nose. *Journal of Applied Physiology* 1993; **75**(4):1767–1775.
12. Naftali S, Schroter RC, Shiner RJ, Elad D. Transport phenomena in the human nasal cavity: a computational model. *Annals of Biomedical Engineering* 1998; **26**:831–839.
13. Elad D, Liebenthal R, Wenig BL, Einav S. Analysis of air flow patterns in the human nose. *Biomedical Engineering* 1993; **31**:585–592.
14. Naftali S, Rosenfeld M, Wolf M, Elad D. The air-conditioning capacity of the human nose. *Annals of Biomedical Engineering* 2005; **33**(4):545–553.
15. Elad D, Naftali S, Rosenfeld M, Wolf M. Physical stresses at the air–wall interface of the human nasal cavity during breathing. *Journal of Applied Physiology* 2006; **100**(3):1003–1010.
16. Zahn CT, Roskies RZ. Fourier descriptors for plane closed curves. *IEEE Transactions on Computers* 1972; **c-21**(3):269–281.
17. Berg E, Mahfouz M, Debrunner C, Hoff W. A 2D Fourier approach to deformable model segmentation of 3D medical images. *Proceedings of the IEEE International Symposium on Biomedical Imaging*, Arlington, VA, 2004.
18. Staib LH, Duncan JS. Left ventricular analysis from cardiac images using deformable models. *Proceedings Computers in Cardiology*, Washington, DC, U.S.A., 1988; 427–430.
19. Wang S, Chung MK. Parametrization and classification of closed anatomical curves. *Technical Report*, vol. 1113. Department of Statistics, University of Wisconsin, 2005.
20. Zhu L, Jiang T. Parameterization of 3D brain structures for statistical shape analysis. *Proceedings of SPIE*, vol. 5370, San Diego, CA, U.S.A., 2004; 1254–1261.
21. El-Faramawy NM, Rangayyan RM, Desautels JEL, Alim OA. Shape factors for analysis of breast tumors in mammograms. *Canadian Conference on Electrical and Computer Engineering*, vol. 1, Calgary, Canada, 1996; 355–358.
22. Rangayyan RM, El-Faramawy NM, Desautels JEL, Alim OA. Measures of acutance and shape for classification of breast tumors. *IEEE Transactions on Medical Imaging* 1997; **16**(6):799–810.
23. Comaniciu D, Meer P, Foran DJ. Image-guided decision support system for pathology. *Machine Vision and Applications* 1999; **11**(4):213–224.
24. Gambaruto AM. Form and flow in anatomical conduits: bypass graft and nasal cavity. *Ph.D. Thesis*, Aeronautics Engineering, Imperial College, 2007.
25. Tebbutt G. Nasal flow and geometry. *M.E. Thesis*, Aeronautics Engineering, Imperial College, 2006.
26. Ohtake Y, Belyaev AG, Bogaevski IA. Polyhedral surface smoothing with simultaneous mesh regularization. *Geometric Modeling and Processing 2000*: *Theory and Applications*, Hong Kong, China, 2000; 229–237.
27. Floater MS. Parameterization and smooth approximation of surface triangulations. *Computer Aided Geometric Design* 1997; **14**(3):231–250.
28. Kobbelt L, Campagna S, Vorsatz J, Seidel PH. Interactive multi-resolution modeling on arbitrary meshes. *Proceedings of the International Conference on Computer Graphics and Interactive Techniques*, Orlando, U.S.A., 1998; 105–114.
29. Desburn M, Meyer M, Schröder P, Barr AH. Implicit fairing of irregular meshes using diffusion and curvature flow. *SIGGRAPH*, Los Angeles, U.S.A., 1999; 317–324.

DOI: 10.1002/fld

30. Giordana S, Sherwin SJ, Peiró J, Doorly DJ, Papaharilaou Y, Caro CG, Watkins N, Cheshire N, Jackson M, Bicknall C, Zervas V. Automated classification of peripheral distal by-pass geometries reconstructed from medical data. *Journal of Biomechanics* 2005; **38**(1):47–62.
31. Carr JC, Fright WR, Beatson RK. Surface interpolation with radial basis functions for medical imaging. *IEEE Transactions on Medical Imaging* 1997; **16**(1):96–107.
32. Trochu F. A contouring program based on dual Kriging interpolation. *Engineering with Computers* 1993; **9**: 160–177.
33. Iske A. Optimal distribution of centres for radial basis function methods. *Report TUM-M0004*, Technische Universität München, 2000.
34. Turk G, O'Brien JF. Shape transformation using variational implicit functions. *Proceedings of the International Conference on Computer Graphics and Interactive Techniques*, Los Angeles, U.S.A., 1999; 335–342.
35. Buhmann MD. *Radial Basis Functions*: *Theory and Implementations*. Cambridge University Press: Cambridge, 2003.
36. Wahba G. *Spline Models for Observational Data*. SIAM CBMS-NSF Regional Conference Series in Applied Mathematics, vol. 59. SIAM: Philadelphia, PA, 1990.
37. Bloomenthal J. An implicit surface polygonizer. *Graphics Gems IV*. Academic Press Professional: Boston, 1994; 324–349.
38. Sonka M. *Image Processing*, *Analysis and Machine Vision*. Chapman and Hall Computing. Chapman & Hall: London, 1995.
39. Jähne B. *Digital Image Processing*. Springer: Berlin, 2002.
40. Hahn I, Scherer PW, Mozell MM. Velocity profiles measured for airflow through a large-scale model of the human nasal cavity. *Journal of Applied Physiology* 1993; **75**(5):2273–2287.
41. Doorly DJ, Taylor DJ, Gambaruto AM, Schroter RC, Tolley N. Nasal architecture: form and flow. *Philosophical Transactions of the Royal Society*, *A* 2008; DOI: 10.1098/rsta.2008.0083.
42. Keyhani K, Scherer PW, Mozell MM. A numerical model of nasal odorant transport for the analysis of human olfaction. *Journal of Theoretical Biology* 1997; **186**:279–301.
43. Fluent Inc. *Fluent*: *Flow Modeling Software*. Fluent Inc.: Lebanon, U.S.A. Available from: http://www.fluent.com.
44. Fluent Inc. *TGrid*: *Unstructured Volume Meshing*. Fluent Inc.: Lebanon, U.S.A. Available from: http://www.fluent.com.
45. Taylor DJ, Doorly DJ, Schroter RC. Inflow boundary profile prescription for numerical simulation of nasal airflow. *Journal of Biomechanics*, submitted.
46. Kelly JT, Prasad AK, Wexler AS. Detailed flow patterns in the nasal cavity. *Journal of Applied Physiology* 2000; **89**:323–337.
47. Croce C, Fodil R, Durand M, Sbirlea-Apioy G, Caillibotte G, Papon J, Blondeau J, Coste A, Isabey D, Louis B. In vitro experiments and numerical simulations of airflow in realistic nasal airway geometry. *Annals of Biomedical Engineering* 2006; **34**(6):997–1007.
48. Morgan KT, Monticello TM. Airflow, gas deposition, and lesion distribution in the nasal passages. *Environmental Health Perspectives* 1990; **88**:209–218.
49. Besl P, McKay N. A method for registration of 3-D shapes. *IEEE Transactions on Pattern Analysis and Machine Intelligence* 1992; **14**(2):239–256.
50. Rusinkiewicz S, Levoy M. Efficient variants of the ICP algorithm. *Third International Conference on 3D Digital Imaging and Modeling*, Quebec City, Canada, 2001.
51. Doorly D, Taylor DJ, Franke P, Schroter RC. Experimental investigation of nasal airflow. *Proceedings of the Institution of Mechanical Engineers*, *Part H*, *Journal of Engineering in Medicine* 2008; DOI: 10.1243/09544119JEIM330.
52. Zhao K, Dalton P, Yang GC, Scherer PW. Numerical modeling of turbulent and laminar airflow and odorant transport during sniffing in the human and rat nose. *Chemical Senses* 2006; **31**:107–118.
53. Finck M, Hanel D, Wlokas I. Simulations of nasal flow by lattice Boltzmann methods. *Computers in Biology and Medicine* 2007; **37**:739–749.